Materialia 6 (2019) 100328

Contents lists available at ScienceDirect

Materialia

journal homepage: www.elsevier.com/locate/mtla

Full Length Article

A generalized spherical harmonics-based procedure for the interpolation of partial datasets of orientation distributions to enable crystal mechanics-based simulations

Timothy J. Barrett[a], Adnan Eghtesad[a], Rodney J. McCabe[b], Bjørn Clausen[b], Donald W. Brown[b], Sven C. Vogel[b], Marko Knezevic[a,*]

[a] Department of Mechanical Engineering, University of New Hampshire, 33 Academic Way, Kingsbury Hall, W119, Durham, NH 03824, USA
[b] Materials Science and Technology Division, Los Alamos National Laboratory, Los Alamos, NM 87545, USA

ARTICLE INFO

Keywords:
Orientation distribution function
Constitutive equations
Elasticity
Thermal expansion
Numerical methods

ABSTRACT

Microstructure evolution-based constitutive models in macro-scale simulation tools require statistical microstructure input at each integration point. This paper reports several robust procedures for interpolating orientation distribution functions (ODFs) from coarsely spaced experimental measurement grids to finely spaced modeling grids. The procedures are based on representing ODFs using generalized spherical harmonics (GSH) functions. Relying on the linearity of the expansion space, the core of the procedures involves weighting of the GSH expansion coefficients over a given variable such as space, strain, or temperature, thus providing ODFs as a function of location, deformation, or thermal treatment. Interpolation approaches including regression and linear/bilinear/barycentric weighting are explored and discussed in terms of their accuracy and suitability. Upon establishing the expansion coefficients of the interpolated ODF, a linear programing problem is solved within the expansion space to construct the interpolated ODF. The procedures are applied to a comprehensive data set obtained by neutron diffraction for a hemispherical part made of depleted α-uranium. Utilizing the ODF interpolation procedures, texture is interpolated over the part revealing significant anisotropy in the texture dependent thermal expansion and elastic stiffness coefficients. The results of this work facilitate introducing thermal expansion and elastic anisotropy into numerical tools for simulating thermo-mechanical loading of microstructurally heterogeneous components using the ODF informed crystal mechanics-based models to more accurately estimate the effective properties required by such simulations.

1. Introduction

Modeling the behavior of polycrystalline metal components subjected to thermal and mechanical loading during processing or service conditions requires spatially resolved computational techniques [1–6]. In order to reveal critical aspects of anisotropic material behavior, knowledge of the spatial distributions of microstructural features is necessary. Crystallographic texture is such a feature and can be quantitatively described by an orientation distribution function (ODF) [7], which is the normalized probability density associated with the occurrence of a given crystal orientation in the polycrystal. Since the orientations of the crystals making up the polycrystalline aggregate govern anisotropic properties such as elastic stiffness and thermal expansion, in particular for highly anisotropic low symmetry metals, knowledge of the orientation distribution allows for an estimate of the bulk properties based on known single crystal properties.

Finite element (FE) method-based numerical simulations that embed texture at finite element material points have been developed [8–15]. Of particular interest for the present development is the FE implementation of the elasto-plastic self-consistent (FE-EPSC) crystal plasticity model [16,17], which is capable of predicting homogenized thermal expansion, elasticity, and plasticity [18]. The FE-EPSC model is able to predict spatial variation of anisotropic deformation because it accounts for spatial variation of crystal lattice orientations of constituent grains and their inherent single crystal anisotropy across FE integration points.

Accurate FE models of components are best constructed based on experimental characterization of position-dependent microstructure. However, experimental measures of microstructures are generally limited to a finite number of positions within a component due to the nature of characterization efforts by electron, X-ray, or neutron-based texture measurements. For predictive modeling capabilities, a considerably finer FE grid/mesh spacing is necessary than is possible to

* Corresponding author.
E-mail address: marko.knezevic@unh.edu (M. Knezevic).

https://doi.org/10.1016/j.mtla.2019.100328
Received 7 April 2019; Accepted 15 April 2019
Available online 18 April 2019

experimentally measure. While it is comparably straight-forward to interpolate scalar, vector, or tensor quantities, interpolation schemes of the mathematically much more complex ODFs are much more involved. Thus, the construction of finely spaced material points considering the spatial variation of the ODF within models based on more coarsely spaced experimental datasets is an important task needing to be addressed.

In recent works [19,20], we presented a rigorous procedure for reducing large datasets of crystal orientations using generalized spherical harmonics (GSH) functions. The procedure involved matching the expansion coefficients of an ODF containing any number of crystal orientations with those of an ODF containing a predetermined compact set of discrete orientations. The linearity of the expansion space was exploited to set a linear programming problem to match the expansion coefficients of the given ODF with those of a compact ODF by varying the weights of orientations in the compact ODF. The compact ODF was then used to model ODF-property relationships and their evolution in crystal plasticity simulations. A number of works reported the GSH representation of ODF-sensitive mechanical properties in an effort to accelerate homogenizations of ODF-effective properties or property bounds [21–27].

In this paper, we develop a GSH-based interpolation methodology to interpolate partial datasets of orientation distributions from a coarse experimental grid of texture measurements to a finite element mesh resolution grid. In the description that follows, the term interpolation will be used to describe both interpolation methodologies and regression methods. These methods advantageously exploit the linearity of the GSH expansion space to interpolate expansion coefficients over space, strain, or temperature. Upon interpolation, an ODF corresponding to the interpolated coefficients at a given point in space is constructed by solving the linear programing problem in the expansion space [19]. We verify this procedure by comparing with an available quaternion interpolation approach [28,29]. We then apply it to a hemispherical component of depleted α-uranium (α-U) with orthorhombic crystal structure for which a comprehensive experimental texture dataset is obtained by spatially resolved neutron diffraction texture measurements. Neutron diffraction measures textures averaged over mm^3 to cm^3 volumes due to the deep penetration of thermal neutrons into most materials combined with beam spot sizes of ~0.1–1 cm^2. This is especially beneficial for the bulk characterization of high atomic number (Z) materials, for which electrons and X-rays have limited penetration and the characterization is therefore limited to near the surface [30].

It is shown that the interpolation procedure developed here is robust and can be used for initializing finite element models based on more limited experimental datasets. This is a novel and unique approach for interpolating orientation distributions. Significant changes in the spatially resolved tensorial components for thermal expansion and elastic stiffness are revealed by interpolating texture over the hemispherical part of α-U, indicating that the predicted distortion with temperature of the part is strongly anisotropic. Such simulations can only be carried out accurately with the knowledge of single crystal constants and the texture at each finite element integration point.

2. Methodologies for interpolation of partial datasets of orientation distributions

This section summarizes two methodologies for texture interpolation. A procedure involving quaternions has been developed [28] and used in the literature for finding an orientation between two crystal orientations [29]. We use it here as a reference to compare and verify the proposed GSH-based procedure for the interpolation of ODFs.

An ODF, $f(g)$, is a probability density function describing the occurrence of a crystal lattice orientation, g, in a volume of a polycrystalline material. The function is appropriately normalized to be expressed as:

$$f(g)dg = \frac{dV}{V}, \int_{OS} f(g)dg = 1, \tag{1}$$

where V is the total volume and dV is the volume increment corresponding to all grains falling within the dg increment in Bunge-Euler space. The OS stands for the orientation space encompassing all orientations [7,31]. An ODF can be defined using a discrete set of crystal lattice orientations, which can be described by a set of three independent variables such as Euler angles e.g. in Bunge notation [7], an angle-axis pair [32], a Rodriguez vector [33], or quaternions [34]. In this work, we will rely on either three Euler angles in Bunge notation $g = (\varphi_1, \Phi, \varphi_2)$ or a set of unit quaternion vector components $\mathbf{q} = (q_1, q_2, q_3, q_4)$ to describe a crystal orientation.

2.1. Quaternion procedure

Taking advantages of the spherical linear interpolation (‘*slerp*’) method [28,29], the quaternion description facilitates a convenient way for interpolating between two crystal orientations. Specifically, the slerp method interpolates along an arc between two quaternions on the unit hypersphere using the following equation:

$$\mathbf{q}_f(t) = \mathbf{q}_1 \frac{\sin((1-t)\theta)}{\sin(\theta)} + \mathbf{q}_2 \frac{\sin(t\theta)}{\sin(\theta)} \tag{2}$$

where $\mathbf{q}_f$ is the final interpolated quaternion, t is a fraction defining the weighted average of the first quaternion ($\mathbf{q}_1$) and the second quaternion ($\mathbf{q}_2$), and θ is the angle between the two quaternions calculated using:

$$\theta = \cos^{-1}\left(\mathbf{q}_1 \cdot \mathbf{q}_2\right) \tag{3}$$

In order to interpolate an ODF, each orientation within the ODF must be interpolated individually from its initial to its final state, which make an input pair of quaternions for the interpolation in the quaternion space. Consequently, the two ODFs must be represented using the same number of discrete orientations. The collection of discrete orientations obtained by interpolating the pairs is the final interpolated ODF. The method has been well established and utilized in several prior studies [29,35], especially in those involving the interpolation between two ODFs experiencing the same or a similar deformation path. While the interpolation involving quaternions is convenient, two interpolated ODFs may not always contain the same number of discrete orientations or may not always evolve from one to another as a consequence of evolution during plastic deformation. Thus, the method is rather restricted to modeling textures. The method would also break down when twinning abruptly reorients a fraction of a crystal rather than gradual reorientation of the entire crystal by slip or in recrystallization. To relax these constraints, other methods based on probability distribution interpolation techniques can be explored and utilized [36–41]. The next section describes procedures for the interpolation of orientation distributions developed in this work.

2.2. GSH procedure

Contrary to the interpolation between pairs of orientations in the previous section, the interpolation/regression procedures developed in this section rely on representing an ODF using GSH expansion coefficients. These coefficients represent a given ODF as a point in GSH expansion space. The procedures developed here find an interpolated ODF (output from the procedures) by interpolating between points representing measured ODFs (input to the procedures). To facilitate representation of the ODF by a finite set of orientations, e.g. as input into an EPSC model we perform an approximation of the interpolated ODF from the coefficients to a weighted set of discrete crystal orientations using a recently developed methodology involving the GSH representation of the ODF [20]. Here, a linear programming problem is solved using the Matlab built in function, *linprog*, which moves the weighted average of the coefficients in a predetermined set of random orientations by adjusting their weights to match the interpolated ODF point in the expansion space, as will be described below.

2.2.1. Representation of ODFs

The harmonic series representation used in this procedure follows the formulation of Bunge as described in [7]. In this formulation, the ODF is represented by a GSH series in the form:

$$f(g) = \sum_{l=0}^{\infty} \sum_{m=-l}^{+l} \sum_{n=-l}^{+l} F_l^{mn} T_l^{mn}(g), \tag{4}$$

where, F_l^{mn} and $T_l^{mn}(g)$ are the expansion coefficients and the GSH function, respectively. Reduction of the expansion series is possible by taking advantage of crystal and sample symmetries. For example, the symmetrized expansion series for orthorhombic-orthotropic[1] symmetry is [7]:

$$f(g) = \sum_{l=0}^{\infty} \sum_{\mu=1}^{M(l)} \sum_{\nu=1}^{N(l)} F_l^{\mu\nu} \ddot{T}_l^{\mu\nu}(g), \tag{5}$$

where $\ddot{T}_l^{\mu\nu}(g)$ is the symmetrized GSH function. The number of triplet (l, ν, μ) combinations defines the number of dimensions of the expansion space. Each triplet corresponds to one expansion coefficient and therefore the number of triplets allowed by symmetry up to the chosen order for the expansion determines the dimensionality of the space. The expansion in the present work is chosen to be $l = 16$. Note that $l = 16$ is the default for the EDAX orientation imaging microscopy (OIM) analysis software, TexSEM Laboratories (TSL). Pertaining to the nomenclature of the symmetrized GSH function, the first column of dots above T represents crystal symmetry (orthorhombic), while the second column of dots represents sample symmetry (orthotropic), and no dots at the given location represent no symmetry i.e. triclinic symmetry [7,20].

Expansion coefficients for an individual orientation g_k in an ODF containing a number of discrete orientations are evaluated using the complex conjugated $\ddot{T}*_l^{\mu\nu}$ as [7]

$${}^{k}F_l^{\mu\nu} = (2l+1)\ddot{T}*_l^{\mu\nu}(g_k). \tag{6}$$

The coefficients ${}^{k}F_l^{\mu\nu}$ for a given orientation g_k can be visualized as a point in the multidimensional expansion space defined by (l, ν, μ) triplet. When Eq. (6) is applied to a set of selected individual crystal orientations, it is used to construct a texture hull. The hull is made up of points corresponding to the expansion coefficients of these orientations. Any empty space between the points in the hull can be filled using a weighted combination of the existing points, g_k. As a result, the hull is convex and a compact representation of the complete set of all physically realizable ODFs. The hull is in the core of the compact reconstruction of interpolated ODFs to get weighted Bungle-Euler angles, as will be described later.

Eq. (6) also applies to any given ODF to obtain a point in the hull after calculating the volume average of the expansion coefficients corresponding to the individual crystal orientations within the given ODF. Here, a given ODF described by a finite set of N_{crys} orientations weighted by weights α is be represented as a point in the hull

$$\bar{F}_l^{\mu\nu} = \sum_{k=1}^{N_{crys}} {}^{k}\alpha\, {}^{k}F_l^{\mu\nu}, \quad \sum_{k=1}^{N_{crys}} {}^{k}\alpha = 1, 0 < {}^{k}\alpha < 1. \tag{7}$$

The bar placed on top of F indicates that the coefficients have been weighted. The weighting of coefficients corresponds to weighting of the crystal orientations belonging to the given ODF. Thus, the linearity of the expansion space facilitates the representation of a single crystal orientation as well as a weighted polycrystalline ODF.

The interpolation/regression of ODFs is accomplished using the averaged expansion coefficients ($\bar{F}_l^{\mu\nu}$) to create a target point in the expansion space. The subsequent generation of a compact ODF corresponding to the target point is accomplished using the hull points (${}^{k}F_l^{\mu\nu}$), as described next.

[1] The first symmetry refers to symmetry at the crystal level, while the second symmetry refers to a statistical symmetry at the sample level.

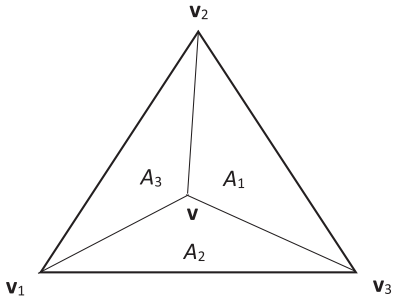

Fig. 1. Simplex showing the areas corresponding to each vertex used to calculate corresponding weights in the Delaunay triangulation.

2.2.2. Interpolation of ODFs

We explore several interpolation methods, each requiring a different number of input ODFs, N. For linear interpolation $N = 2$, for bilinear interpolation $N = 4$, and for barycentric weighting $N = 3$. Note that linear/bilinear/barycentric interpolation belong to the same technique. Interpolation between N ODFs is performed on each expansion coefficient defined by a combination of (μ, ν, l) with respect to a dependent variable such as spatial coordinates, $\mathbf{x}$, or accumulated plastic strain, ε.

Linear interpolation between two ODFs uses the following equation:

$$\hat{F}_l^{\mu\nu}(t) = (1-t)\, {}_1\bar{F}_l^{\mu\nu} + t\, {}_2\bar{F}_l^{\mu\nu}, \; 0 < t < 1 \tag{8}$$

where t is the distance defining the weighted average between expansion coefficients of the first ODF, ${}_1\bar{F}_l^{\mu\nu}$, and expansion coefficients of the second ODF, ${}_2\bar{F}_l^{\mu\nu}$, and $\hat{F}_l^{\mu\nu}$ are the resulting interpolated expansion coefficients. The ODF corresponding to $\hat{F}_l^{\mu\nu}$ can be constructed, as will be explained below.

A two-dimensional (2D) grid of ODFs can be interpolated using bilinear interpolation. Four ODFs are used as an input to interpolate in two spatial dimensions, x and y. For a given point of interest (x, y), bilinear interpolation is performed using:

$$\begin{aligned}\hat{F}_l^{\mu\nu}(x,y) = {} & \frac{(x_2-x)(y_2-y)}{(x_2-x_1)(y_2-y_1)}\, {}_{11}\bar{F}_l^{\mu\nu} + \frac{(x-x_1)(y_2-y)}{(x_2-x_1)(y_2-y_1)}\, {}_{21}\bar{F}_l^{\mu\nu} \\ & + \frac{(x_2-x)(y-y_1)}{(x_2-x_1)(y_2-y_1)}\, {}_{12}\bar{F}_l^{\mu\nu} + \frac{(x-x_1)(y-y_1)}{(x_2-x_1)(y_2-y_1)}\, {}_{22}\bar{F}_l^{\mu\nu}, \\ & y_1 < y < y_2\,,\; x_1 < x < x_2,\end{aligned} \tag{9}$$

where $\hat{F}_l^{\mu\nu}(x,y)$ are the resulting interpolated expansion coefficients, while ${}_{ij}\bar{F}_l^{\mu\nu}$ are the input expansion coefficients at points (x_i, y_j). Bilinear interpolation is linear along each of the edges and inherently quadratic through the 2D space.

When ODF data is available in a highly irregular grid, Delaunay triangulation and barycentric weighting can conveniently be used. The Delaunay triangulation is performed to find a set of triangles, referred to as simplices, that discretize the space. This is done in Matlab using the built in Delaunay function. For a given point of interest $\mathbf{v}(x, y)$, the enclosing simplex and barycentric weights are found using the Matlab function *tsearchn*, which uses the Delaunay triangulation as an input. The areas, A_i, corresponding to each vertex, $\mathbf{v}_i$, are depicted in Fig. 1. The barycentric weights, w_i, of each vertex, are calculated using the following equations

$$w_i = \frac{A_i}{A},\; A = \sum_{i=1}^{3} A_i. \tag{10}$$

The weighted average of the expansion coefficients at each vertex is the target point

$$\hat{F}_l^{\mu\nu} = \sum_{i=1}^{3} w_i\, {}_i\bar{F}_l^{\mu\nu} \tag{11}$$

The barycentric weighting method is continuous throughout the simplex and linear along all edges.

2.2.3. Regression analysis of ODFs

Similar to interpolation methods, regression analysis can be performed on the expansion coefficients when multiple ODFs area available. This allows more data to be incorporated into the determination of textures between grid points facilitating smoothing, which is usually beneficial. One-dimensional (1D) quadratic regression (local using partial data or global using all data) is performed using the polyfit least-squares regression function in Matlab. A second order polynomial is fit for each expansion coefficient as a function of e.g. spatial position or strain as

$$\hat{F}_l^{\mu\nu} = \bar{P}_l^{\mu\nu} x^2 + \bar{Q}_l^{\mu\nu} x + \bar{R}_l^{\mu\nu}. \tag{12}$$

The coefficients $\bar{P}_l^{\mu\nu}$,$\bar{Q}_l^{\mu\nu}$, and $\bar{R}_l^{\mu\nu}$are fit independently for each dimension (μ, ν, l) with respect to spatial coordinate x or strain level ε.

Two-dimensional (2D), (x, y), quadratic regression is usually done using the locally weighted regression function, 'loess', in Matlab. This function weights points within a user defined span using the tricube function:

$$w_i = \left(1 - \left| \frac{\left(\sqrt{(x - x_i)^2 + (y - y_i)^2} \right)}{d} \right|^3 \right)^3 \tag{13}$$

Where, (x, y) are the predictor values, (x_i, y_i) are the nearest neighbors, and d is the furthest distance from the predictor value within the span. For this work, 20 spatial points were used for each regression. Symmetry can be introduced to include more data at the boundaries and improve regression quality.

A locally weighted 2nd order regression (i.e. quadratic *LOESS*) is performed on each of the expansion coefficients to determine the target point.

$$\hat{F}_l^{\mu\nu} = \bar{P}_l^{\mu\nu} + \bar{Q}_l^{\mu\nu} x + \bar{R}_l^{\mu\nu} y + \bar{S}_l^{\mu\nu} xy + \bar{T}_l^{\mu\nu} x^2 + \bar{U}_l^{\mu\nu} y^2. \tag{14}$$

The variables $\bar{P}_l^{\mu\nu}$, $\bar{Q}_l^{\mu\nu}$, $\bar{R}_l^{\mu\nu}$, $\bar{S}_l^{\mu\nu}$, $\bar{T}_l^{\mu\nu}$, and $\bar{U}_l^{\mu\nu}$ are regression coefficients, which are calculated by minimizing the weighted residuals. If the residual of a data point is more than six times the median absolute deviation of the resulting regression the data point is removed and the regression is repeated. Since texture hull by definition is a convex and compact space representing the complete set of all physically realizable ODFs, the target point must lie within the hull. With the regression methods due to intrinsic nonlinearity, it is possible to generate a target point that is outside of the texture hull and therefore is not physically possible. It is not possible to reconstruct a compact ODF for such a point. In this case another interpolation techniques is used which by default will always produce a target point that is in the hull and is physically possible. It is worth mentioning that regression is not restricted to LOESS. Methods such as 'kriging' [42] have also been explored yielding similar results to those obtained by LOESS. Alternative techniques can easily be implemented into our overall procedure.

2.2.4. Compact reconstruction of interpolated ODFs

After GSH coefficients have been interpolated, as a final step, it is necessary to generate an equivalent compact ODF in the form of Bunge-Euler angles in order to enable crystal mechanics simulations. For computational efficiency of the crystal mechanics simulations, it is desirable for the ODF to be as compact as possible. A compact ODF consisting of a certain number of weighted orientations corresponding to the target point, $\hat{F}_l^{\mu\nu}$, is constructed by solving a linear programming problem [20]. A uniform ODF is conveniently generated in MTEX and the expansion coefficients for each crystal orientation, k, of this uniform ODF, ${}^k F_l^{\mu\nu}$ are calculated. Typically the number of discrete crystal orientations chosen to represent an ODF ($k = 1..K$) is of the order of a few hundred. These orientations are invariant – only their weights change. To initialize the procedure, the weight per orientation, ${}^k\alpha$, is set equal (i.e. $1/K$). Using the built in Matlab function *linprog* a linear programming problem is set to find the weights of each crystal orientation, ${}^k\alpha$, in such a way that the sum of the weighted expansion coefficients of the uniform ODF, ${}^k\alpha {}^k F_l^{\mu\nu}$, evolve to the target $\hat{F}_l^{\mu\nu}$. The only requirement for finding the weights is that the target point, $\hat{F}_l^{\mu\nu}$, must be within the hull of points, ${}^k F_l^{\mu\nu}$. Since the hull is convex and compact, a linear combination of single crystal points is possible, provided that the target point lies within the hull. The system of equations is

$$\hat{F}_l^{\mu\nu} - {}^k\alpha {}^k F_l^{\mu\nu} - W_l^{\mu\nu} = 0, \sum_{k=1}^{N_{crys}} {}^k\alpha = 1 \tag{15}$$

with the inequality constraints

$${}^k\alpha \geq 0, W_l^{\mu\nu} \geq 0 \tag{16}$$

and the objective function to minimize is

$$\sum_{l=0}^{\infty} \sum_{\mu=1}^{M(l)} \sum_{\nu=1}^{N(l)} W_l^{\mu\nu} \tag{17}$$

The slack variable, $W_l^{\mu\nu}$, is necesary for the linprog solver. The linprog function adjusts the weights until a prescribed tolerance is achieved. This tolerance is defined by

$$TOL = \sum_{l=0}^{\infty} \sum_{\mu=1}^{M(l)} \sum_{\nu=1}^{N(l)} |\hat{F}_l^{\mu\nu} - {}^k\alpha {}^k F_l^{\mu\nu}| \tag{18}$$

The tolerance is set to $TOL = 10^{-12}$ to ensure that the sum of the weighted expansion coefficients of the compact ODF are identical to the target point. Once the weights are found, the compact interpolated ODF is available.

2.2.5. Texture difference index

To evaluate the quality of the interpolated textures we introduce the texture difference index (*TDI*). This measure is used to quantify the accuracy of interpolated textures in terms of their spectral representation corresponding to $l = 16$. The *TDI* is calculated using:

$$TDI = \frac{\sum_{l=0}^{\infty} \sum_{\mu=1}^{M(l)} \sum_{\nu=1}^{N(l)} |\bar{F}_l^{\mu\nu} - \hat{F}_l^{\mu\nu}|}{d} \tag{19}$$

where, $\bar{F}_l^{\mu\nu}$ and $\hat{F}_l^{\mu\nu}$ are the expansion coefficients for the target (measured) ODF and compact (interpolated) ODF, respectively. d is the furthest distance between any two points in the convex hull, which is made up of expansion coefficients corresponding to a uniform ODF. The *TDI* as defined in Eq. (19) represents the distance of the interpolated ODF to the measured ODF normalized by the furthest possible distance. This definition bounds the *TDI* between 0 and 1, a *TDI* of 0 corresponds to a perfect fit, while a *TDI* of 1 corresponds to a single crystal on the boundary of the hull at the furthest possible point from the target.

3. Results

3.1. Verification case study: tension and compression of alloy AA6022-T4

The objective of this case study is to interpolate between simulated tension and compression textures deformed to different levels of true strain and to compare the equally weighted tension and compression textures for the given strain level with the initial texture. Texture evolution between true strain levels of 0.1, 0.2, and 0.3 in tension and compression creates the interpolation space with strain as a variable. The largest strain space of 0.6 provides a stringent test for the methodology.

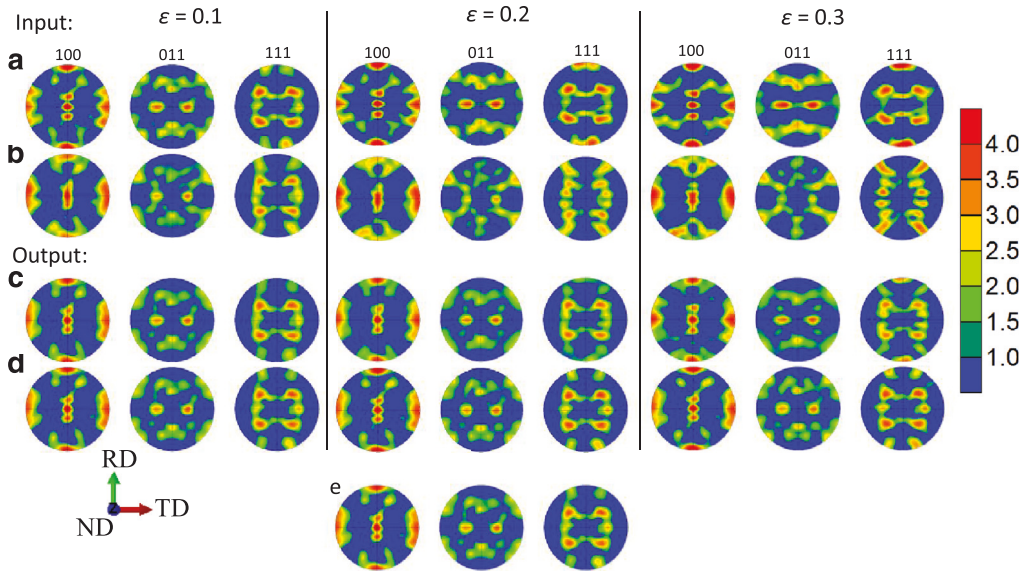

Fig. 2. Pole figures for textures (input): (a) calculated with EPSC for simple tension along RD to the strain levels indicated in the figure and (b) calculated with EPSC for simple compression along RD to the strain levels indicated in the figure. Pole figures for interpolated textures (output) between (a) and (b) for a given strain level using: (c) the GSH procedure with linear interpolation of expansion coefficients and (d) the quaternion procedure. (e) Initial (undeformed) texture.

The case resembles interpolation of texture gradients in a beam exposed to pure bending, where the top of the beam is in compression, the bottom of the beam is in tension, and the middle of the beam is undeformed [11]. Thus, the simulated data for tension and compression mimics spatially resolved texture measurements across a plastically deformed beam subjected to pure bending, which leads to a variation from top to bottom changing from axial tension to axial compression. If the beam is assumed to be long, the non-zero shear deformation between top and bottom of it is small. Fig. 2 shows a set of pole figures obtained by EPSC calculations (Fig. 2a and b for tension and compression, respectively) and based on the interpolation methodologies involving GSH (Fig. 2c) and quaternions (Fig. 2d). The EPSC calculations use the undeformed ODF shown in Fig. 2e as input [43]. In this case study, the GSH procedure is restricted to linear between tension and compression. The texture interpolated for the strain free state between the given strain level in tension and compression is expected to resemble the initial texture (Fig. 2e), since the face-centered cubic Al alloy exhibit approximately symmetric tension vs. compression behavior. The comparison between pole figures in Fig 2e and those obtained using the interpolation procedures in Fig. 2c and d can be used to evaluate the accuracy.

Interpolation using quaternions is always performed between two orientations, in this case one predicted for tension and one predicted for compression to the same magnitude of plastic strain that originated from the same undeformed initial crystal orientation. This approach satisfies two constraints of the quaternion procedure: (1) the texture predicted in tension is represented by the same number of discrete orientations as the texture predicted in compression and (2) pairing between the orientations from the discrete sets is ensured because the same initial crystal orientation evolves in both tension and compression. The interpolated ODF between those evolved in tension and compression corresponds to the initial ODF. Thus, the average of a given ODF evolved a strain step into tension and the same given ODF evolved the same strain amount into compression is the original given ODF. This is only true for the initial texture (ODF) that is symmetric with respect to the loading axes (mirror symmetry on the plane defined by the loading axis) and under slip deformation, as is the case here. To verify the GSH method, we perform the same interpolation. As is evident from comparing the triplet of pole figures in Fig. 2e with the three triplets of Fig. 2c, the linear interpolation of the expansion coefficients loses accuracy with increasing strain, while the strain-free texture interpolated using the quaternion methodology (Fig. 2d) agrees well with the actual initial texture. As explained earlier, the GSH interpolation operates on the entire distribution rather than individual crystal orientations. Furthermore, the use of simulated crystal orientations allowed to assign pairs of quaternions. However, such assignment would not be possible for textures experimentally determined at the same deformation levels. Nevertheless, the case study facilitates evaluation of the accuracy of the GSH method for subsequent interpolation of ODFs that do not contain the same number of discrete orientations and that do not evolve from one to another. The GSH procedure interpolates ODFs as probability distributions, which are represented using the expansion coefficients. Thus, accuracy of the interpolation of the coefficients is the key to the accuracy of the overall ODF interpolation.

Table 1
TDI calculated for each scheme interpolating between compression and tension textures at strain levels of 0.1, 0.2, and 0.3 as compared to the initial undeformed texture.

	$\varepsilon = 0.1$	$\varepsilon = 0.2$	$\varepsilon = 0.3$
Quaternion	0.0038	0.0147	0.0286
Linear interpolation	0.0096	0.0305	0.0541

The accuracy of the interpolation schemes is quantified using the *TDI*. Table 1 shows the *TDI* of the interpolated textures between compression and tension textures at strain levels of 0.1, 0.2, and 0.3 as compared to the initial undeformed texture. This shows rate at which each scheme deteriorates. Two textures with a $TDI < 0.05$ are considered to be in good agreement, and $TDI < 0.03$ represents excellent agreement. The quaternion method produces good results at strain levels up to 0.3, while the GSH interpolation method loses accuracy after $\varepsilon = 0.2$.

Fig. 3 shows for selected coefficients $F_l^{\mu\nu}$ that inherent non-linearity of the GSH expansion coefficients develops with strain. Satisfactory accuracy of the GSH procedure can be achieved even for the strain level of 0.3 by taking into account the non-linearity of the expansion coefficients by making them continuous functions using quadratic regression analysis in 1D. The global regression was performed using data points at ε of ± 0.2 and ± 0.4 as input for interpolation output at ε of 0 and ± 0.3. This is shown in Fig. 4. Note that the bottom row textures in Fig. 4a–c are all

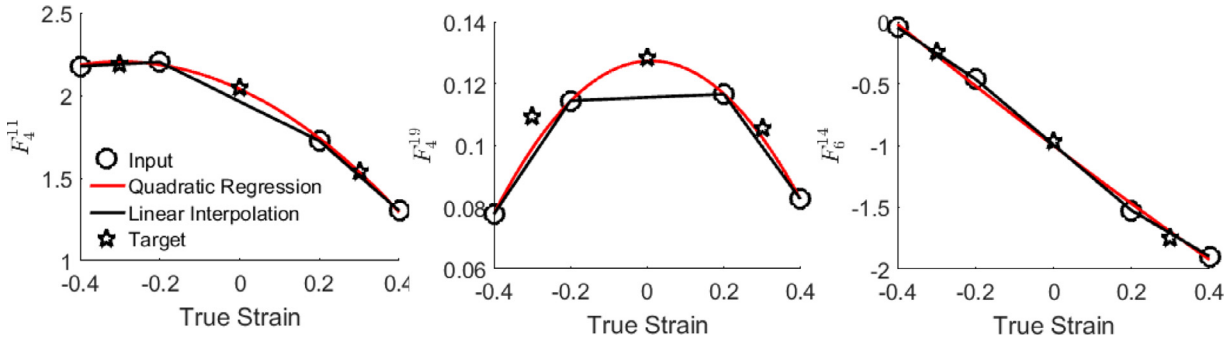

Fig. 3. One-dimensional evolution path with true strain for three selected expansion coefficients F_l^{uv} during simple tension and simple compression along RD of cubic-triclinic texture of AA6022-T4. Input for the interpolation consists of four textures generated using EPSC. The star symbols represent accurate solutions and are also determined using EPSC.

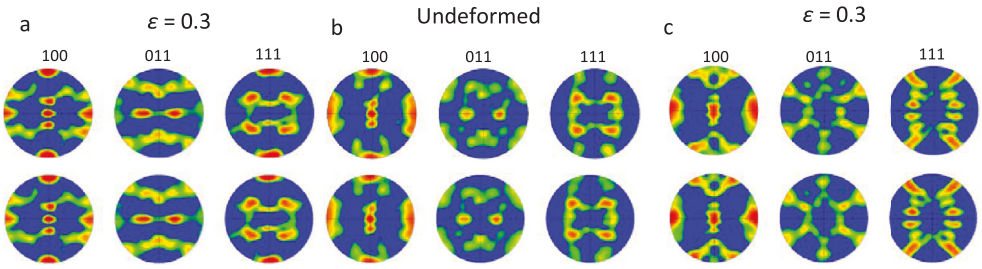

Fig. 4. Pole figures comparing textures obtained using EPSC simulations from Fig. 2 (top row) to those based on the continuous expansion coefficient interpolation (bottom row): (a) texture after simple tension to the strain level indicated in the figure, (b) top - initial (undeformed) texture and bottom – interpolated texture, and (c) texture after compression to the strain level indicated in the figure. The continuous expansion coefficients used to calculate the bottom row pole figures are obtained using the quadratic regression analysis with data at ε of ±0.2 and ±0.4 (Fig. 3). The pole figure frame and the intensity bar showing the multiples of random distribution are the same as those in Fig. 2.

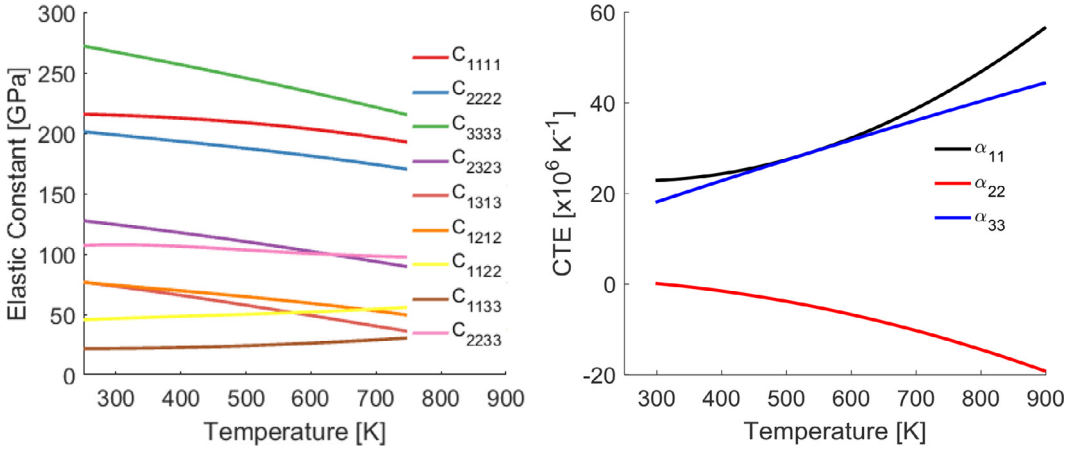

Fig. 5. Single crystal elastic [38] and thermal expansion [39] constants for α-U as a function of temperature.

Table 2
TDI calculated for quadratic regression textures at strain levels of ±0.3 and the initial undeformed texture.

	$\varepsilon = -0.3$	Undeformed texture	$\varepsilon = 0.3$
Quadratic regression	0.0300	0.0291	0.0177

continuously interpolated consistent with Fig. 3. Table 2 shows the *TDI* calculated for each texture, all textures show excellent agreement.

3.2. Application case study: formed α-uranium hemisphere

The texture in a clock-rolled plate of α-U is spatially non-uniform, which leads to anisotropic stiffness and thermal expansion properties. Thermal expansion in particular, shows a strong dependence on texture making it highly relevant for the interpolation study. If such a plate is subjected to a temperature change there would be thermal residual stresses generated. Moreover, if the plate is formed at temperature into a hemisphere, the geometrical constraints imposed by the forming die will not allow the hemisphere to distort freely, and thus the internal residual stresses will be enhanced. Finally, the shape will be non-hemispherical upon removal of the die. In order to predict these distortions and residual stresses using a finite element model the initial spatially varying orientation distribution is needed as input. Fig. 5 shows temperature-dependent single crystal properties of α-U that will be used for calculating the homogenized crystallographic texture sensitive bulk elastic stiffness tensor and thermal expansion tensor properties using the self-consistent approach [16,44]. Since the preferred orientation of the crystals making up the polycrystalline aggregate governs elastic stiffness and thermal expansion, in particular of the highly anisotropic α-U, texture characterization allows for an estimate of these properties in bulk poloycrystals based on the known single crystal properties [45–47] and the

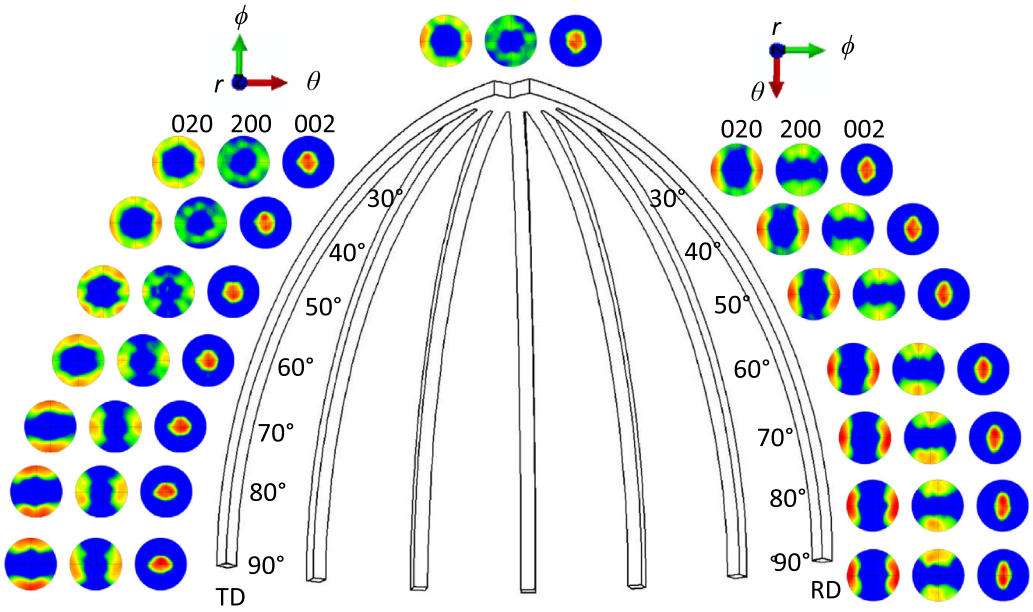

Fig. 6. Schematic of half the arcs as cut from the hemisphere with the polar angles (along arcs) and azimuth (Az) angle (along equator of hemisphere). Measured pole figures are shown for several polar angles along RD (Az = 0°) and TD (Az = 90°). The indicated frame pertains only to pole figures, the pole figure axes are parallel to the azimuthal, polar, and radial directions. The intensity bar showing the multiples of random distribution is the same as in Fig. 2.

spatial orientation distributions. Measurement of these orientation distributions is described next.

3.2.1. Experimental

Spatially resolved texture characterization of a depleted α-U hemisphere was performed using neutron diffraction. The texture measurements were conducted on arc-shaped samples cut from equator to pole of the hemisphere (Fig. 6). The experimental setup consisted of custom made sample holders allowing the arcs to be mounted to the standard sample holders of the robotic sample changer [48] of the High Pressure/Preferred Orientation (HIPPO) beam line [49,50] at the pulsed neutron spallation source at LANSCE [51], which is a neutron time-of-flight diffractometer for bulk microstructural characterization of materials at ambient and non-ambient (temperature, pressure, load etc.) conditions [49–51]. Owing to the 45 detector panels, covering ~25% of the sphere around the sample [52] each sample orientation provides 45 inverse pole figures in a neutron time-of-flight measurement with constant detector locations. The arc samples were measured at angles of −45°, 22.5°, and 45° around the vertical axis. The arcs were rotated and translated to complete the measurement along each arc. The samples were held by a robotic sample changer [48] with pre-programmed angles ensuring that the neutron beam impinged on the arcs in the radial direction when the sample was rotated to 0° vertical rotation angle. This procedure ensures that the reference coordinate system (radial/normal direction, azimuthal and polar directions) was the same for each probed sample volume. A 2 mm cadmium slit, a strong thermal neutron absorber, was installed in front of the samples to limit the illuminated volume to a 2 mm radial slice of the arc. The count time was 20 min (at full proton accelerator current, slightly longer typically), leading to about one hour of beam time per probed volume on an arc (i.e. polar increment) or about 9 h total per arc with measurements occurring at 10° polar increments along the arcs. A total of 121 texture measurements were made on arcs representing half of the hemisphere. Rolled Cu sheet, with a known orthorhombic texture symmetry was glued to the arcs and the texture of this phase was analyzed simultaneously. In case of a misorientation of the arc with respect to the reference coordinate system, the symmetry of the texture of the rolled Cu sheet would have been destroyed. This phase thus provided a check of the orientation of each slice of the uranium arc.

Data analysis consisted of simultaneous Rietveld refinements against all collected histograms (three times 44 histograms, one detector defective) with procedures described in detail in [53,54]. No texture symmetry was imposed. The ODF was represented by the E-WIMV method [55] with a 7.5° resolution. The measuring coordinate system is such that the pole figures would have the radial outer surface at the top vertically, the radially inner surface at the bottom vertically, and the azimuthal circumference at constant polar angle left/right horizontally. The center of the pole figures is therefore the polar circumference. Later, pole figures are rotated for presentation in their local frame to have their radial direction at the center, polar direction horizontally, and azimuthal direction vertically (spherical coordinate system).

Fig. 6 shows a schematic of the arcs as cut from the hemisphere along with α-U pole figures for two arcs in 10° polar increments. The pole figures at the north pole of the hemisphere, measured from a piece cut from that location, are at the top. The pole figures are contoured in multiples of random distribution (mrd), i.e. a pole density of 5 indicates a five times higher pole density than for a sample with random crystal orientations. As is evident, the α-U pole figures show a strong preferred orientation of (002) poles (**c**-axes) towards the radial direction of the arc segment. At the north pole, the (020) poles (**b**-axes) are preferably oriented along the prior RD of the rolled plate that was formed into the hemisphere [56–58]. The **b**-axes are preferably oriented along the polar circumference and the (200) poles (**a**-axes) are preferably oriented along the azimuthal direction. It can be seen that the **b**-axes tend to align along the major tensile direction during the forming operation. The equator of the hemisphere was effectively subjected in tension along the polar circumference during the forming operation, which in turn means that going from the north pole along the prior RD axis shows a small development of the (020) pole density, but going from the north pole to the equator along other than the RD axis shows a significant variation of the (020) pole density. This disparity in texture variation along different polar circumferential directions is what would generate internal stresses and distortions during a temperature change of the hemisphere. Due to the axisymmetric forming process, the pole figures at the equator are approaching a single component orientation, where the **c**-axes are preferentially along the radial direction, the **b**-axes are preferentially along the polar circumference, and the **a**-axes are preferentially along the azimuthal circumference.

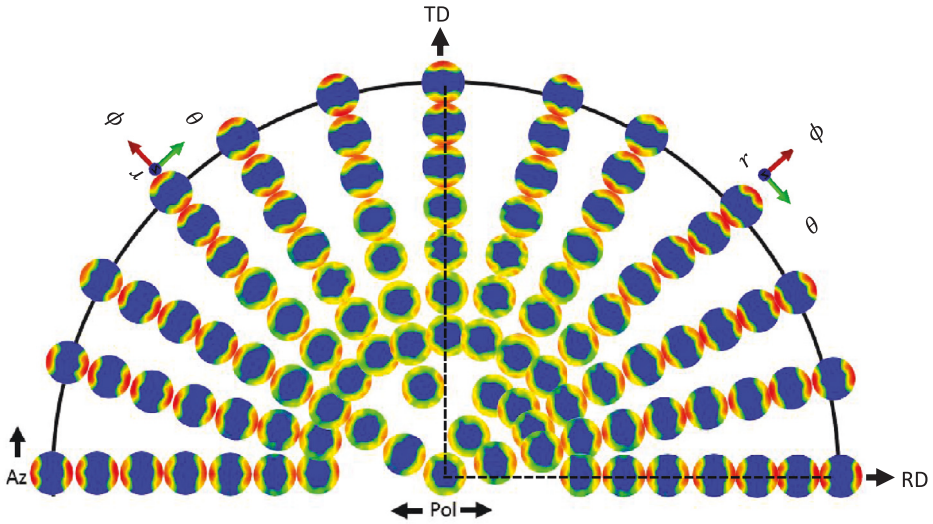

Fig. 7. Projected {020} poles measured by neutron diffraction on a hemisphere made of depleted α-U plotted in measured frame defined by azimuthal direction (θ), polar direction (ϕ), and radial direction (r). The dashed lines pass through pole figures shown in Fig. 6. The intensity bar showing the multiples of random distribution is the same as in Fig. 2.

The {020} pole figures for all measured textures are plotted in Fig. 7. The objective of clock-rolling is to produce an axi-symmetric texture with regard to the plate ND. However, process variations always result in some texture asymmetry, and this is usually most obvious in the presence of an {020} peak somewhere about the periphery of the pole figure (ND normal). The {020} peak is a convenient texture reference and we use a common convention of orienting the position of the {020} peak as the RD of the plate. The {020} pole reveals a clear peak alignment with the polar circumference showing significant texture evolution due to forming.

3.2.2. Calculations

The developed GSH texture interpolation procedure is applied to the measured data presented in the previous section. The data collected in 10° polar and 15° azimuthal increments represents a coarse (sparse) grid requiring a substantial refinement to facilitate initializing a finite element model of the hemispherical part for crystal mechanics-based thermo-mechanical simulations. Data was only measured for half of the hemisphere. We assume orthotropic sample symmetry and rotate the data 180° around the ND two-fold symmetry axis for each measured point. At the equator of the hemisphere, we assume no symmetry.

Fig. 8a shows calculated normal components of the thermal expansion tensor at 25 °C for all measured textures, i.e. on the discrete grid of the texture measurement. The predicted shear components of the thermal expansion tensor are orders of magnitude smaller than the normal components and omitted here. The crystal values are homogenized using the self-consistent approach in EPSC and are shown in the local spherical frame. Fig. 8a reveals the texture effects of the thermal expansion values. Similarly, Fig. 8b depicts the values for three shear components of the elastic stiffness tensor at 25 °C calculated using EPSC. These were chosen due to their strong texture dependence.

Fig. 9 shows several projections of the texture hull for α-U. Since the interpolation is performed between measured texture data, consideration of the entire texture hull is not necessary. Consequently, the α-U hemisphere sub-space in the hull is delineated based on the measured data. Since the α-U hemisphere contains a small sub section of all physically realizable textures, the corresponding sub-space is smaller.

Orientation distributions can be used in the upper bound homogenization theory to obtain predictions of bounds for the effective properties. These rigorous first-order bounds using the orientation distribution are readily available, especially for the diagonal components of the elastic stiffness and thermal expansion tensors. The upper bound for these components is evaluated as the volume average over single crystals [59–62]. To verify that the linear interpolation between two textures corresponds to the linear interpolation in these properties, we equally weighted textures in Fig. 10a and c to get b and calculate the properties. The average texture in Fig. 10b is obtained by averaging the expansion coefficients of the pole cap and RD Pol 30 textures. The average expansion coefficients are used to construct the averaged texture. The volume average calculated properties for the three textures are provided in Table 3 and are regarded as the upper bound. The upper bound properties for texture in Fig. 10b can be alternatively calculated as the average between the values for textures in Fig. 10a and c. The small percent difference between the values based on the averaged texture and those based on averaging the values validates the GSH texture interpolation methodology in the linear expansion space. However, our objective is to use more accurate estimates of the effective properties than upper bound. We rely on the EPSC model for the calculation of effective properties. With the texture information, we can additionally calculate the reorientation of the grains and the change in the elastic coefficients throughout a forming simulation.

Pole figures showing the results of spatial 1D texture interpolation based on the linear method and the regression analysis along RD in 2.5° increments are shown in Fig. 11. Pole figures corresponding to input textures are boxed in on the left. The nearest 20 neighbors are used as input textures for the regression method. Qualitatively, the peaks in the interpolated/regressed textures appear to be correct.

Fig. 12 shows values for the selected components of thermal expansion and elastic stiffness tensors in the local frame computed for the azimuthal, radial, and polar direction using EPSC for the textures in Fig. 11 i.e. as a function of polar angle from the pole cap (0°) to the equator (90°) along Az = 0. As is evident, significant changes in the values occur that can only be computed with knowledge of the bulk texture and the single crystal properties. The plot includes values based the measured orientation distributions and two interpolation methods. The linear interpolation of ODFs results in a linear distribution of thermal expansion and elastic stiffness coefficients between measured data points. The regression method provides similar values to the linear interpolation method for polar angles greater than 10° with the addition of curvature between points. For polar angles less than 10°, the pole cap values are smoothed out due to weighting by the surrounding points. Although the pole figure intensities in Fig. 7 seem to be continuous functions of position on the hemisphere (the texture changes smoothly), the texture at the pole cap is a discontinuity causing some deviations for the LOESS analysis. This is due to the fact that as the pole cap is approached, there is a numerical singularity where textures having polar circumfer-

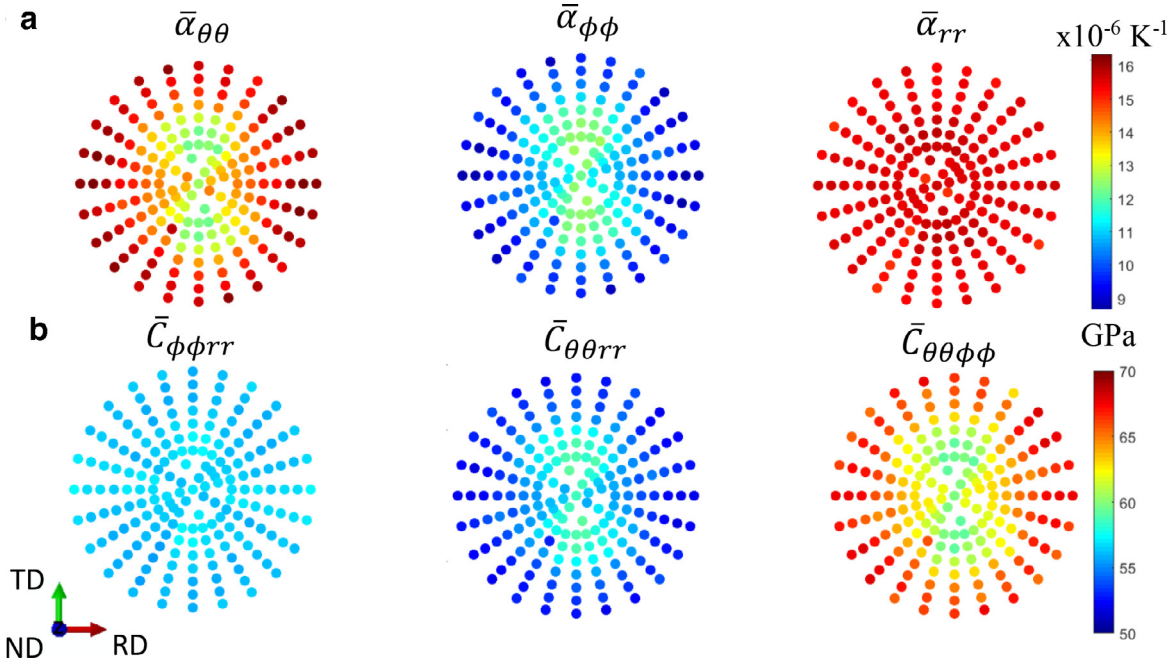

Fig. 8. Predicted (a) thermal expansion coefficients and (b) elastic stiffness tensor components at 25 °C for each measured texture.

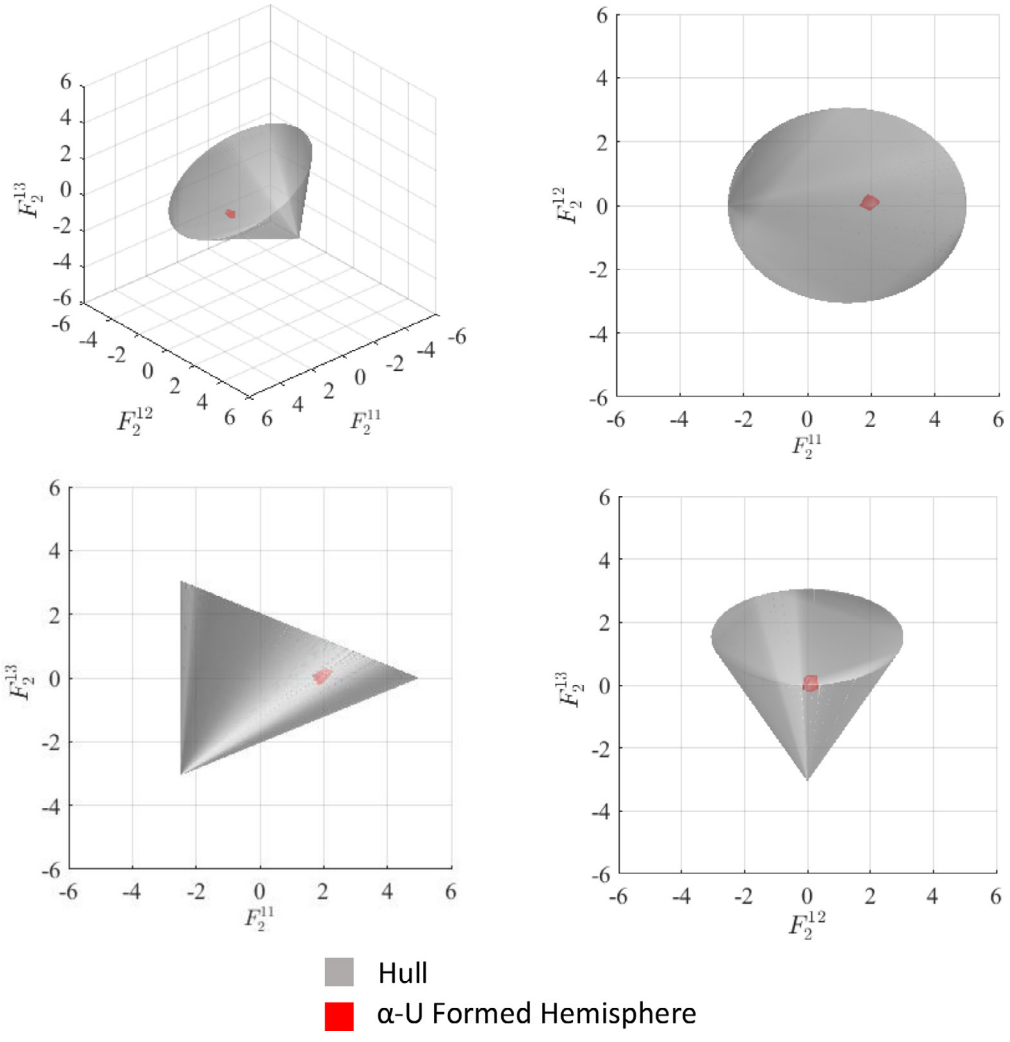

Fig. 9. A texture hull for orthorhombic-triclinic ODFs in the first three dimensions of the expansion space containing the sub hull made up of the α-U hemisphere textures.

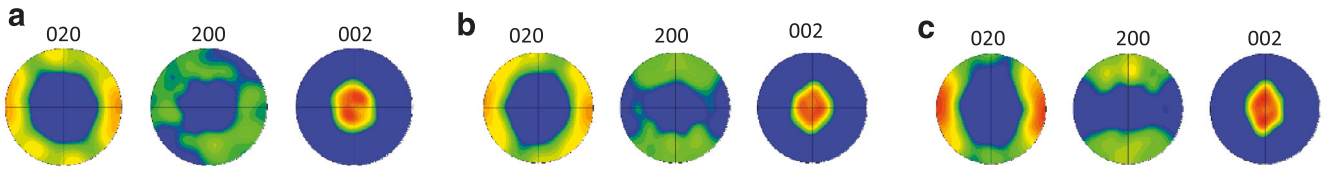

Fig. 10. Global sample frame pole figures showing (a) the measured pole cap texture, (b) the linearly interpolated texture half way between (a) and (c), and (c) the measured texture at a polar angle of Pol = 30° along the RD axis (Az = 0°). The intensity bar and the pole figure frame are the same as in Fig. 2.

Table 3
Selected upper bound (i.e. the volume weighted average over crystal values) thermal expansion and elastic stiffness tensor components evaluated for the pole cap texture (Fig. 10a), RD Pol30 (Fig. 10c) texture, and the averaged texture (Fig. 10b). The coefficient average is obtained by averaging the values for the pole cap and RD Pol30 textures to determine the percent difference between the coefficient average and the ODF average results.

	$\bar{\alpha}_{\theta\theta}$ [x10^6 K^{-1}]	$\bar{\alpha}_{\phi\phi}$ [x10^6 K^{-1}]	$\bar{\alpha}_{rr}$ [x10^6 K^{-1}]	$\bar{C}_{\phi\phi rr}$ [GPa]	$\bar{C}_{\theta\theta rr}$ [GPa]	$\bar{C}_{\theta\theta\phi\phi}$ [GPa]
Pole cap	12.6474	11.6624	16.8247	56.93	59.15	59.15
RD Pol30	14.1903	10.2823	16.6619	56.89	55.56	63.14
Texture average	13.4188	10.9723	16.7433	56.90	57.41	61.11
Coefficient average	13.4343	10.9544	16.7458	56.91	57.36	61.15
% difference	0. 12	0. 16	0. 015	0.01	0.1	0.06

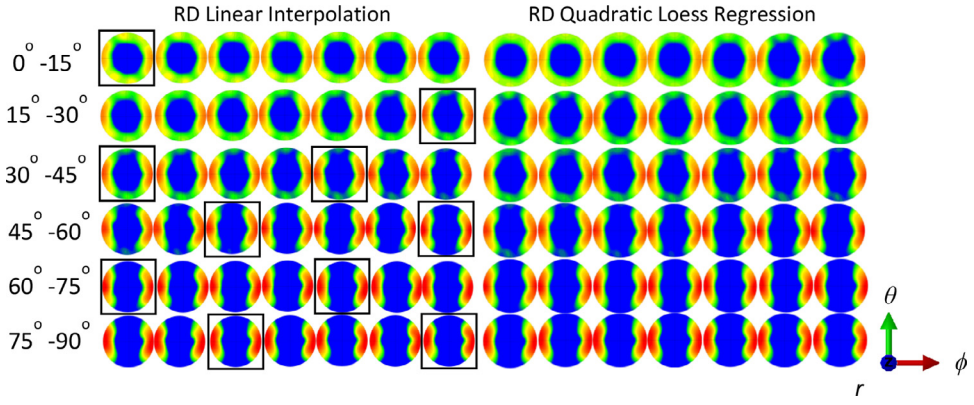

Fig. 11. {020} pole figures along RD in 2.5° increments. Linearly interpolated textures are on the left and quadratic loess regressed textures are on the right. Pole figures corresponding to input textures are boxed in on the left. The nearest 20 neighbors (in all directions) are used as input textures for quadratic regression on the right. The intensity bar showing the multiples of random distribution is the same as in Fig. 2.

ence directions originally aligned with the RD evolve much faster. During the forming process there is a combined bending and tension stress state along the polar circumference of the hemisphere. There is also a state of compression along the azimuthal circumference. These states of mechanical fields drive the texture evolution. Works like [63,64], have shown the strong dependence of texture evolution on the compression direction for α-U. As a result, the textures near the pole cap vary substantially with the probing direction, while the pole cap texture is invariant experiencing only rigid motion. It is this difference in texture evolution that leads to the numerical singularity that is seen at the pole cap causing oscillations in the LOESS smoothing. It is important to note that the regression method does not necessarily produce the same texture as a measured texture at the measurement position whereas an interpolated texture necessarily does.

Fig. 13 shows pole figures comparing results obtained based on the LOESS regression and bilinear interpolation methods with experimental measurements. The coordinates for each pole figure are specified by the values of Az and Pol in the figure. Input textures for the bilinear interpolation scheme are distinguished with boxes. The particular section of the hemisphere depicting the comparisons was chosen due to the large texture gradient observed. Interpolation/regression is most accurate where gradients are small making this the most difficult section for validation. Note that interpolation along the edges of measured points reduces to 1D linear interpolation for bilinear and barycenric interpolation, while 3** and 4 are the only interpolated textures influenced by the data in 2D. All of the textures labeled 3 in Fig 13 were produced using bilinear interpolation, but the same results would be obtained if barycentric interpolation were used. Input textures for the quadratic LOESS regression includes the 20 nearest neighbors excluding the five experimentally measured textures for a fair comparison and validation. These five excluded textures are denoted by 1*. Considering these textures in the analysis would improve the results. As explained earlier, the regression method does not always produce the same measured textures at the coordinates of measured textures. For this reason we also show the resulting regressed textures for four of the input textures, which are denoted by 1. The *TDI* of each of the resulting textures as compared to the experimental data is shown in Table 4. For the input textures the *TDI* for bilinear and barycentric interpolation is 0, while there is a small difference for the LOESS regression textures. At the data points excluded from the interpolation and regression the average *TDI* is 0.00684 and 0.00694, respectively. The negligibly small *TDI* confirms excellent agreement.

Finally, thermal expansion coefficients at room temperature based on textures interpolated to a uniform 1°x1° grid over the hemisphere are shown in Fig. 14. This level of refinement is similar to what would be seen on a finite element mesh for the same part. For Fig. 14a, texture for each material point is obtained by interpolating the measured data using barycentric weighting at the irregular grid of texture data for $\phi < 30°$ and bilinear weighting at the regular grid of texture data for $\phi \geq 30°$. For Fig. 14b, textures for each material point obtained by

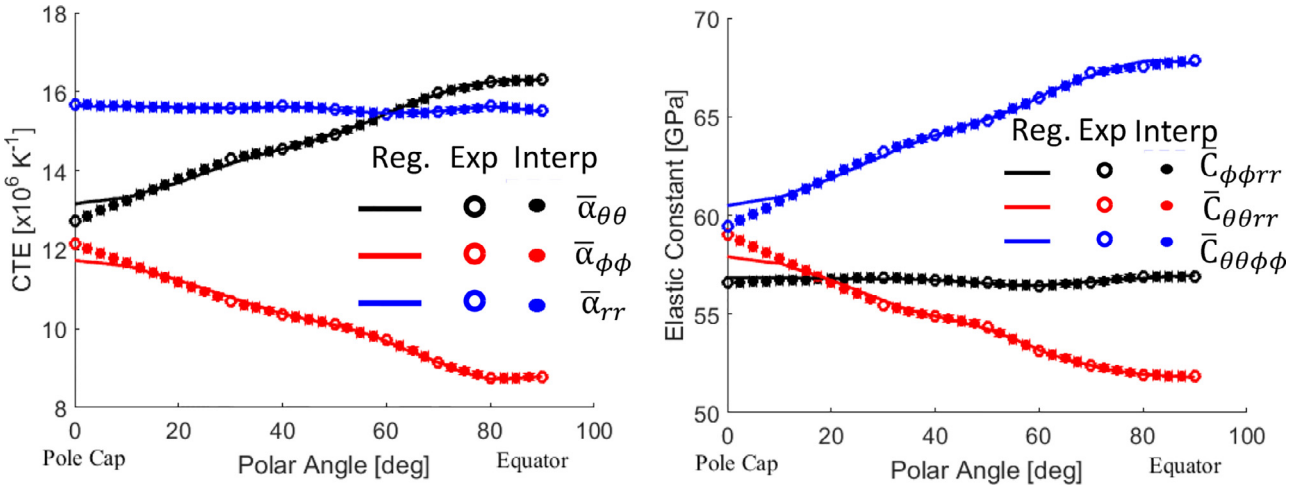

Fig. 12. Predicted coefficients of thermal expansion (CTE) and selected components of elastic stiffness tensor at room temperature for textures in Fig. 11. The circles, stars and lines are plotted using experimentally measured textures, linearly interpolated textures, and regressed textures, respectively.

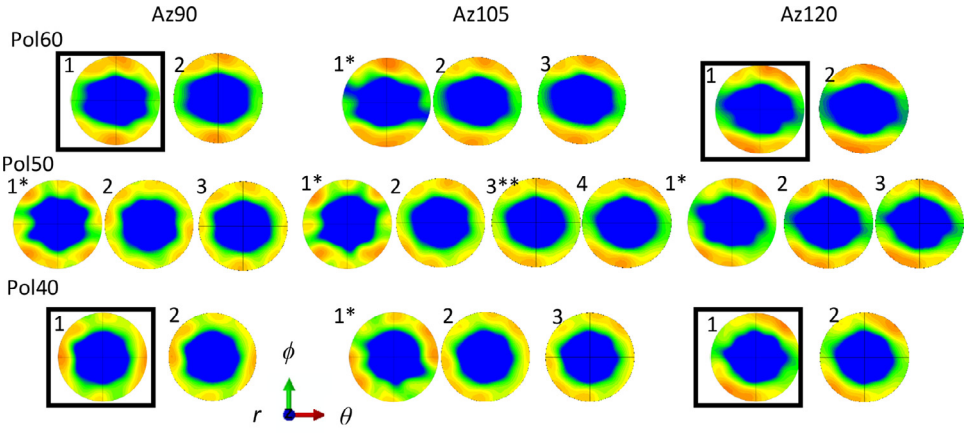

Fig. 13. {020} pole figures showing the comparison between 1) measured and calculated by 2) quadratic loess regression, 3) two-dimensional bilinear interpolation, and 4) barycentric interpolation. The coordinates for each pole figure are specified by the values of Az and Pol. Input textures for the quadratic loess regression include the 20 nearest neighbors excluding 1* textures. Input textures for the bilinear interpolation scheme are 1 and are boxed in. The intensity bar is the same as in Fig. 2.

Table 4
TDI calculated for each interpolation technique as compare to the measured texture.

	Az90 Pol40	Az90 Pol50	Az90 Pol60	Az105 Pol40	Az105 Pol50	Az105 Pol60	Az120 Pol40	Az120 Pol50	Az120 Pol60
Barycentric	0	0.0079	0	0.0066	0.0084	0.0055	0	0.0058	0
Bilinear	0	0.0079	0	0.0066	0.0084	0.0055	0	0.0058	0
Loess	0.0029	0.0082	0.0028	0.0062	0.0087	0.0054	0.0041	0.0062	0.0029

quadratic LOESS regression. The coefficients of thermal expansion are calculated using the self-consistent method available in EPSC. As is evident, both methods produce reasonably smooth continuous distributions between measured data points. However, the LOESS regression has smoother contours while the bilinear interpolation matches the measured data exactly.

4. Discussion

This work explores several interpolation methods between experimental datasets of orientation distributions taking advantage of the linear expansion space of GSH to enable crystal mechanics-based finite element thermo-mechanical simulations. The procedure is first validated against an established procedure involving quaternions and then applied to a case study of α-U. The interpolation procedure involving quaternions is convenient for interpolating between ODFs having the same number of discrete orientations that evolved from one to another. Advantageously, the new GSH procedure developed here is a probability distribution interpolation technique. Comprehensive texture data forming orientation distributions at experimental grid points is collected by neutron diffraction and presented for a hemispherical, α-U part. Data refinement by interpolation is necessary to initialize a finite element mesh of the same part.

The detailed analysis revealed that filtering out rigid rotations should be done before performing interpolation/regression to minimize differences between textures and that the quadratic LOESS regression method is the most appropriate of the explored methods for refining data in 1D and 2D. The added benefit of LOESS regression is 'outlier' detection and data smoothing from large deviations. The fact that LOESS regression does not necessarily match the measured data exactly is a benefit of the technique, as the regression can be considered to lie within the experimental uncertainty/error. While regression analysis is often successful, it is possible that it will generate a target point that is outside of the texture hull that is physically inadmissible. This could happen if the amount

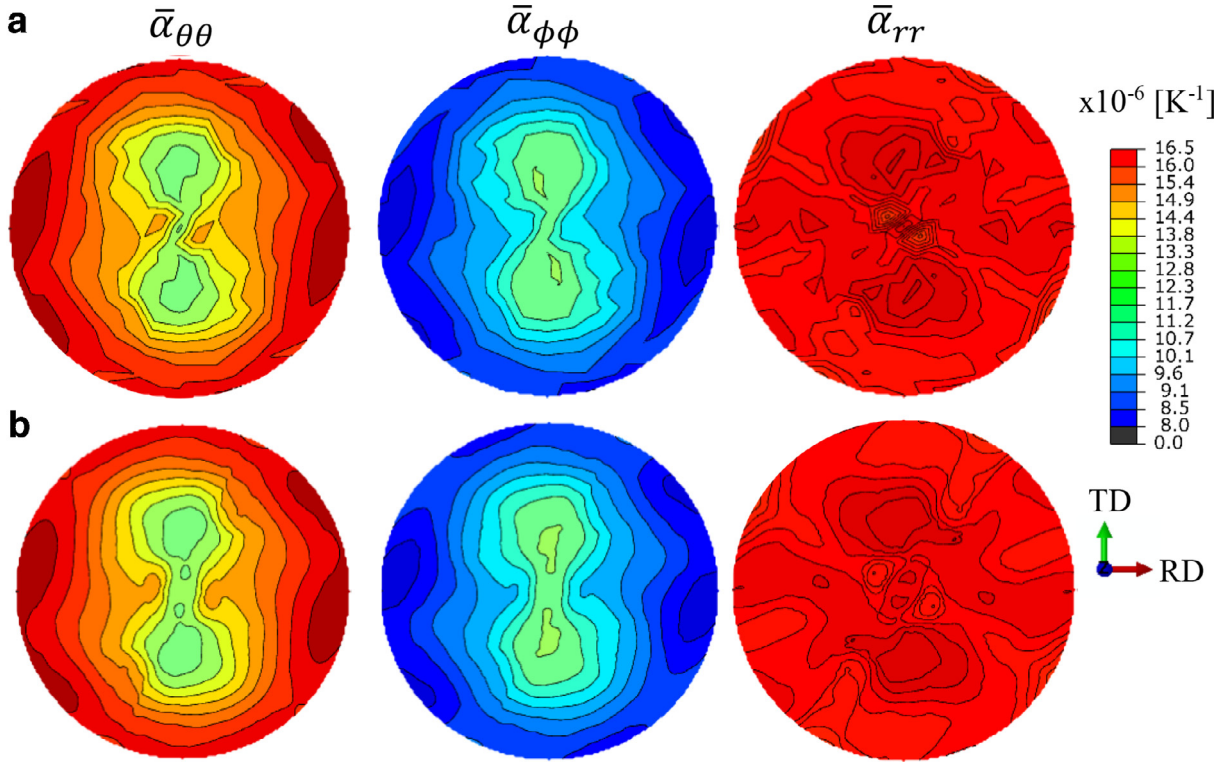

Fig. 14. Predicted thermal expansion coefficients at room temperature based on textures at each material point after a) interpolation using barycentric weighting at the irregular grid of texture data for $\phi < 30^{\circ}$ and bilinear weighting at the regular grid of texture data for $\phi \geq 30^{\circ}$ and b) loess regression weighting.

of measured data is insufficient or if the data contains many outliers. In this case the linear interpolation method should be used, as it will always produce a target point that is in the hull as physically possible. The linear/bilinear/barycentric weighting always match the measured data, even if the measured data contains outliers. In this study, all regressions produced coefficients lie within the texture hull.

5. Conclusions

This paper develops a robust procedure for the interpolation of orientation distributions aimed at initializing FE models embedding ODF sensitive and crystal mechanics-based constitutive models. The procedure is based on representing ODFs using GSH functions into the linear expansion space of the weighting coefficients. At the core of the procedure is weighting of the expansion coefficients of ODFs within the linear expansion space of GSH. Several approaches including the linear, bilinear, regression and barycentric weighting are explored to perform the interpolation. It is found that the quadratic LOESS regression method is the most appropriate for weighting and simultaneous smoothing of sufficiently large experimental data sets. While linear/bilinear/barycentric interpolation also successfully refine measured data, this method is recommended for small sets of experimental data, where the regression may be statistically insignificant. Upon establishing the expansion coefficients of the interpolated ODF, a linear programing problem is solved within the expansion space to construct the interpolated ODF. The procedure is applied to interpolate a comprehensive data set obtained by neutron diffraction for a hemispherical part made of depleted α-U. It is shown that the procedure is robust and can be used for initializing finite element models. Significant changes in the torsional components for thermal expansion and elastic stiffness are revealed by plotting these properties over the hemispherical part of α-U meaning that the predicted distortion with temperature of the part are strongly anisotropic. Heating/cooling simulations of parts made of α-U can now be carried out more accurately because material properties based on texture and single crystal constants are available at each FE integration point.

Acknowledgments

T.J. B., A.E., and M.K. gratefully acknowledge support from the U.S. National Science Foundation under grant no. CMMI - 1650641. T.J.B also wishes to acknowledge support from the G.T. Seaborg Institute through the Seaborg Summer Research Fellowship Program. S.C.V., B.C., D.W.B., and R.J.M. acknowledge support by the U.S. Department of Energy through the Los Alamos National Laboratory for the characterization of the uranium hemisphere at LANSCE. Los Alamos National Laboratory is operated by Triad National Security, LLC, for the National Nuclear Security Administration of the U.S. Department of Energy under contract number 89233218NCA000001.

Declaration of interest

None.

Supplementary material

Supplementary material associated with this article can be found, in the online version, at doi:10.1016/j.mtla.2019.100328.

References

[1] A. Eghtesad, T.J. Barrett, K. Germaschewski, R.A. Lebensohn, R.J. McCabe, M. Knezevic, OpenMP and MPI implementations of an elasto-viscoplastic fast Fourier transform-based micromechanical solver for fast crystal plasticity modeling, Adv. Eng. Softw. 126 (2018) 46–60.

[2] A. Eghtesad, M. Zecevic, R.A. Lebensohn, R.J. McCabe, M. Knezevic, Spectral database constitutive representation within a spectral micromechanical solver for computationally efficient polycrystal plasticity modelling, Comput. Mech. 61 (2018) 89–104.

[3] M. Ardeljan, I.J. Beyerlein, M. Knezevic, A dislocation density based crystal plasticity finite element model: application to a two-phase polycrystalline HCP/BCC composites, J. Mech. Phys. Solids 66 (2014) 16–31.

[4] S. Ghorbanpour, M. Zecevic, A. Kumar, M. Jahedi, J. Bicknell, L. Jorgensen, I.J. Beyerlein, M. Knezevic, A crystal plasticity model incorporating the effects of precipitates in superalloys: application to tensile, compressive, and cyclic deformation of Inconel 718, Int. J. Plast. 99 (2017) 162–185.

[5] M. Zecevic, I.J. Beyerlein, R.J. McCabe, B.A. McWilliams, M. Knezevic, Transitioning rate sensitivities across multiple length scales: microstructure-property relationships in the Taylor cylinder impact test on zirconium, Int. J. Plast. 84 (2016) 138–159.

[6] M. Zecevic, M.V. Upadhyay, E. Polatidis, T. Panzner, H. Van Swygenhoven, M. Knezevic, A crystallographic extension to the Olson-Cohen model for predicting strain path dependence of martensitic transformation, Acta. Mater. 166 (2019) 386–401.

[7] H.-J. Bunge, Texture Analysis in Materials Science, Mathematical Methods, Cuvillier Verlag, Göttingen, 1993.

[8] M. Knezevic, R.J. McCabe, R.A. Lebensohn, C.N. Tomé, C. Liu, M.L. Lovato, B. Mihaila, Integration of self-consistent polycrystal plasticity with dislocation density based hardening laws within an implicit finite element framework: application to low-symmetry metals, J. Mech. Phys. Solids 61 (2013) 2034–2046.

[9] S.R. Kalidindi, C.A. Bronkhorst, L. Anand, Crystallographic texture evolution in bulk deformation processing of FCC metals, J. Mech. Phys. Solids 40 (1992) 537–569.

[10] M. Zecevic, M. Knezevic, modeling of sheet metal forming based on implicit embedding of the elasto-plastic self-consistent formulation in shell elements: application to cup drawing of AA6022-T4, JOM 69 (2017) 922–929.

[11] M. Knezevic, R.A. Lebensohn, O. Cazacu, B. Revil-Baudard, G. Proust, S.C. Vogel, M.E. Nixon, Modeling bending of α-titanium with embedded polycrystal plasticity in implicit finite elements, Mater. Sci. Eng. A 564 (2013) 116–126.

[12] M. Knezevic, M. Jahedi, Y.P. Korkolis, I.J. Beyerlein, Material-based design of the extrusion of bimetallic tubes, Comput. Mater. Sci. 95 (2014) 63–73.

[13] M. Ardeljan, I.J. Beyerlein, B.A. McWilliams, M. Knezevic, Strain rate and temperature sensitive multi-level crystal plasticity model for large plastic deformation behavior: application to AZ31 magnesium alloy, Int. J. Plast. 83 (2016) 90–109.

[14] M. Ardeljan, M. Knezevic, Explicit modeling of double twinning in AZ31 using crystal plasticity finite elements for predicting the mechanical fields for twin variant selection and fracture analyses, Acta. Mater. 157 (2018) 339–354.

[15] M. Ardeljan, I.J. Beyerlein, M. Knezevic, Effect of dislocation density-twin interactions on twin growth in AZ31 as revealed by explicit crystal plasticity finite element modeling, Int. J. Plast. 99 (2017) 81–101.

[16] P.A. Turner, C.N. Tomé, A study of residual stresses in Zircaloy-2 with rod texture, Acta Metall. Mater. 42 (1994) 4143–4153.

[17] M. Zecevic, M. Knezevic, A dislocation density based elasto-plastic self-consistent model for the prediction of cyclic deformation: application to Al6022-T4, Int. J. Plast. 72 (2015) 200–217.

[18] M. Zecevic, I.J. Beyerlein, M. Knezevic, Coupling elasto-plastic self-consistent crystal plasticity and implicit finite elements: applications to compression, cyclic tension–compression, and bending to large strains, Int. J. Plast. 93 (2017) 187–211.

[19] M. Knezevic, N.W. Landry, Procedures for reducing large datasets of crystal orientations using generalized spherical harmonics, Mech. Mater. 88 (2015) 73–86.

[20] A. Eghtesad, T.J. Barrett, M. Knezevic, Compact reconstruction of orientation distributions using generalized spherical harmonics to advance large-scale crystal plasticity modeling: verification using cubic, hexagonal, and orthorhombic polycrystals, Acta. Mater. 155 (2018) 418–432.

[21] P. Van Houtte, Fast calculation of average Taylor factors and Mandel spins for all possible strain modes, Int. J. Plast. 17 (2001) 807–818.

[22] M. Knezevic, S.R. Kalidindi, Fast computation of first-order elastic-plastic closures for polycrystalline cubic-orthorhombic microstructures, Comput. Mater. Sci. 39 (2007) 643–648.

[23] X. Wu, G. Proust, M. Knezevic, S.R. Kalidindi, Elastic-plastic property closures for hexagonal close-packed polycrystalline metals using first-order bounding theories, Acta. Mater. 55 (2007) 2729–2737.

[24] T. Fast, M. Knezevic, S.R. Kalidindi, Application of microstructure sensitive design to structural components produced from hexagonal polycrystalline metals, Comput. Mater. Sci. 43 (2008) 374–383.

[25] J.B. Shaffer, M. Knezevic, S.R. Kalidindi, Building texture evolution networks for deformation processing of polycrystalline fcc metals using spectral approaches: applications to process design for targeted performance, Int. J. Plast. 26 (2010) 1183–1194.

[26] M. Knezevic, S.R. Kalidindi, R.K. Mishra, Delineation of first-order closures for plastic properties requiring explicit consideration of strain hardening and crystallographic texture evolution, Int. J. Plast. 24 (2008) 327–342.

[27] M. Knezevic, H.F. Al-Harbi, S.R. Kalidindi, Crystal plasticity simulations using discrete Fourier transforms, Acta. Mater. 57 (2009) 1777–1784.

[28] K. Shoemake, Animating Rotation with Quaternion Curves, ACM SIGGRAPH computer graphics, 19, ACM, 1985, pp. 245–254.

[29] A. Prakash, W.G. Nöhring, R.A. Lebensohn, H.W. Höppel, E. Bitzek, A multiscale simulation framework of the accumulative roll bonding process accounting for texture evolution, Mater. Sci. Eng. A 631 (2015) 104–119.

[30] S.C. Vogel, A review of neutron scattering applications to nuclear materials, ISRN Mater. Sci. 2013 (2013) 1–24.

[31] S.R. Kalidindi, M. Knezevic, S. Niezgoda, J. Shaffer, Representation of the orientation distribution function and computation of first-order elastic properties closures using discrete Fourier transforms, Acta. Mater. 57 (2009) 3916–3923.

[32] F.C. Frank, Orientation mapping, MTA 19A (1987) 403–408.

[33] P. Neumann, Representation of orientations of symmetrical objects by Rodrigues vectors, Textures Microstruct. 14-18 (1991) 53–58.

[34] Y. Takahashi, K.i. Miyazawa, M. Mori, Y. Ishida, Quaternion representation of the orientation relationship and its application to grain boundary problems, Trans. Jpn. Inst. Met. 27 (1985) 345–352.

[35] M. Zecevic, M. Knezevic, A new visco-plastic self-consistent formulation implicit in dislocation-based hardening within implicit finite elements: application to high strain rate and impact deformation of tantalum, Comput. Methods Appl. Mech. Eng. 341 (2018) 888–916.

[36] B.E. Hollister, A. Pang, Interpolation of non-Gaussian probability distributions for ensemble visualization, in: Proceedings of the IEEE VIS Posters, 2013.

[37] N. Bonneel, M. Van De Panne, S. Paris, W. Heidrich, Displacement interpolation using Lagrangian mass transport, ACM Trans. Graph. TOG 30 (2011) 158.

[38] F.H. Bursal, On interpolating between probability distributions, Appl. Math. Comput. 77 (1996) 213–244.

[39] V. Sundararaghavan, N. Zabaras, Linear analysis of texture–property relationships using process-based representations of Rodrigues space, Acta Materialia 55 (2007) 1573–1587.

[40] M. Miller, T. Turner, A methodology for measuring and modeling crystallographic texture gradients in processed alloys, Int. J. Plast. 17 (2001) 783–805.

[41] S. Gribbin, J. Bicknell, L. Jorgensen, I. Tsukrov, M. Knezevic, Low cycle fatigue behavior of direct metal laser sintered Inconel alloy 718, Int. J. Fatigue 93 (Part 1) (2016) 156–167.

[42] M. Strano, Optimization under uncertainty of sheet-metal-forming processes by the finite element method, Proc. Inst. Mech. Eng. Part B J. Eng. Manuf. 220 (2006) 1305–1315.

[43] M. Zecevic, M. Knezevic, Latent hardening within the elasto-plastic self-consistent polycrystal homogenization to enable the prediction of anisotropy of AA6022-T4 sheets, Int. J. Plast. 105 (2018) 141–163.

[44] P. Lipinski, M. Berveiller, Elastoplasticity of micro-inhomogeneous metals at large strains, Int. J. Plast. 5 (1989) 149–172.

[45] E.S. Fisher, Temperature dependence of the elastic moduli in alpha uranium single crystals, part IV (298 to 923K), J. Nuclear Mater. 18 (1966) 39–54.

[46] Y.S. Touloukian, R. Kirby, R. Taylor, P. Desai, Thermophysical Properties of Matter-the TPRC Data Series, 12, Thermophysical and Electronic Properties Information Analysis Center Lafayette IN, New York, NY, USA, 1975 Thermal Expansion Metallic Elements and Alloys.

[47] M. Knezevic, J. Crapps, I.J. Beyerlein, D.R. Coughlin, K.D. Clarke, R.J. McCabe, Anisotropic modeling of structural components using embedded crystal plasticity constructive laws within finite elements, Int. J. Mech. Sci. 105 (2016) 227–238.

[48] A.S. Losko, S.C. Vogel, H.M. Reiche, H. Nakotte, A six-axis robotic sample changer for high-throughput neutron powder diffraction and texture measurements, J. Appl. Crystallogr. 47 (2014) 2109–2112.

[49] H.-R. Wenk, L. Lutterotti, S. Vogel, Texture analysis with the new HIPPO TOF diffractometer, Nuclear Instrum. Methods Phys. Res. Sect. A Accel. Spectrom. Detect. Assoc. Equip. 515 (2003) 575–588.

[50] S.C. Vogel, C. Hartig, L. Lutterotti, R.B. Von Dreele, H.-R. Wenk, D.J. Williams, Texture measurements using the new neutron diffractometer HIPPO and their analysis using the Rietveld method, Powder Diffr. 19 (2004) 65–68.

[51] P.W. Lisowski, K.F. Schoenberg, The Los Alamos neutron science center, Nuclear Instrum. Methods Phys. Res. Sect. A Accel. Spectrom. Detect. Assoc. Equip. 562 (2006) 910–914.

[52] S. Takajo, S.C. Vogel, Determination of pole figure coverage for texture measurements with neutron time-of-flight diffractometers, J. Appl. Crystallogr. 51 (2018) 895–900.

[53] J. Pehl, S. Matthies, H.R. Wenk, S. Vogel, L. Lutterotti, Quantitative texture analysis with the HIPPO neutron TOF diffractometer, J. Appl. Crystallogr. 38 (2005) 462–475.

[54] H.-R. Wenk, L. Lutterotti, S. Vogel, Rietveld texture analysis from TOF neutron diffraction data, Powder Diffr. 25 (2010) 283–296.

[55] S. Matthies, L. Lutteroti, H. Wenk, Advances in texture analysis from diffraction spectra, J. Appl. Crystallogr. 30 (1997) 31–42.

[56] M. Knezevic, L. Capolungo, C.N. Tomé, R.A. Lebensohn, D.J. Alexander, B. Mihaila, R.J. McCabe, Anisotropic stress-strain response and microstructure evolution of textured a-uranium, Acta. Mater. 60 (2012) 702–715.

[57] R.J. McCabe, A.W. Richards, D.R. Coughlin, K.D. Clarke, I.J. Beyerlein, M. Knezevic, Microstructure effects on the recrystallization of low-symmetry alpha-uranium, J. Nucl. Mater. 465 (2015) 189–195.

[58] M. Knezevic, R.J. McCabe, C.N. Tomé, R.A. Lebensohn, S.R. Chen, C.M. Cady, G.T. Gray Iii, B. Mihaila, Modeling mechanical response and texture evolution of α-uranium as a function of strain rate and temperature using polycrystal plasticity, Int. J. Plast. 43 (2013) 70–84.

[59] E. Kroner, Bounds for effective elastic moduli of disordered materials, J. Mech. Phys. Solids 25 (1977) 137–155.

[60] R. Hill, The elastic behavior of a crystalline aggregate, Proc. R. Soc. Lond. Ser. A Math. Phys. Sci. 65 (1952) 349–354.

[61] B. Paul, Prediction of elastic constants of multiphase materials, Trans. Metall. Soc. AIME 218 (1960) 36–41.

[62] N. Landry, M. Knezevic, Delineation of first-order elastic property closures for hexagonal metals using fast fourier transforms, Materials 8 (2015) 6326–6345.

[63] M. Zecevic, M. Knezevic, I.J. Beyerlein, R.J. McCabe, Origin of texture development in orthorhombic uranium, Mater. Sci. Eng. A 665 (2016) 108–124.

[64] M. Zecevic, M. Knezevic, I.J. Beyerlein, R.J. McCabe, Texture formation in orthorhombic alpha-uranium under simple compression and rolling to high strains, J. Nucl. Mater. 473 (2016) 143–156.